AAS 16-235

GROUND-BASED NAVIGATION AND DISPERSION ANALYSIS FOR THE ORION EXPLORATION MISSION 1

Christopher D'Souza[*], Greg Holt[†], Renato Zanetti[‡], and Brandon Wood[§]

This paper presents the Orion Exploration Mission 1 Linear Covariance Analysis for the DRO mission using ground-based navigation. The $|\Delta \mathbf{V}|$ statistics for each maneuver are presented. In particular, the statistics of the lunar encounters and the Entry Interface are presented.

INTRODUCTION

This paper presents the navigation and dispersion analysis for the Orion Exploration Mission 1 (EM-1) Distant Retrograde Orbit (DRO) mission with ground-based navigation. It is based upon the theory presented in Maybeck.[1] This is a further analysis of the DRO trajectory along the lines of what was presented by D'Souza and Zanetti.[2]

The accuracy of the flight-path angle at Entry Interface[††] (EI) is driven by several factors including the navigation, targeting, and burn execution errors at the time of the last mid-course maneuver, and unaccounted trajectory perturbations between the last mid-course maneuver and EI. Apollo missions tolerated a maximum flight path angle error at EI of ± 1 degree, with half of this error allocated to navigation. A similar criterion is employed in this study.

Perturbations are a major source of errors in the cislunar navigation performance of Orion. In a perfect world all the sources of perturbations would be modeled in the filter dynamics. However, computational limitations (and fundamental knowledge) preclude such extensive modeling. Therefore, the primary sources of perturbations are characterized. In particular there are three categories of unmodeled acceleration: propulsive sources, gravitational perturbations, and solar radiation pressure. Only propulsive errors are included in this analysis; the gravitational and solar radiation pressure are not included; they will be included in a future study. For EM-1, the gravitational and solar radiation pressure errors are several orders of magnitude below the thrusting sources. The propulsive sources considered are: attitude deadbands, attitude slews, CO_2 venting, and sublimator venting.

Linear covariance techniques are used to perform the analysis for the Orion Cislunar missions. This comports well for the navigation system design since the cislunar navigation system on Orion will be an Extended Kalman Filter. Many of the same states and dynamics used in the linear covariance analysis will be used in the on-board cislunar navigation system. A preliminary design of

[*]GNC Autonomous Flight Systems Engineer, EG6, NASA Johnson Space Center, Houston, TX 77058
[†]Flight Dynamics Engineer, Flight Operations Directorate, CM44, NASA Johnson Space Center, Houston, TX 77058
[‡]GNC Autonomous Flight Systems Engineer, EG6, NASA Johnson Space Center, Houston, TX 77058
[§]Pathways Intern, GNC Autonomous Flight Systems Branch, Johnson Space Center, Houston, TX 77058
[††]For Orion Entry Interface is normally taken to be at an altitude of 400,000 ft.

the cislunar navigation system is presented. This is supported by linear covariance analyses which provides navigation performance, trajectory dispersion performance and $|\Delta\mathbf{V}|$ usage.

The paper is organized as follows: Section 2 will contain a brief description of linear covariance analysis. In Section 3, the navigation system will be described, both the filter dynamics as well as the measurement. Section 4 will contain results of this analysis. Finally, a few concluding comments are made in Section 5.

LINEAR COVARIANCE ANALYSIS

This investigation is performed using linear covariance (LinCov) analysis techniques.[1,3] The state vector is

$$\mathbf{x} = \begin{Bmatrix} \mathbf{r}^{\mathrm{T}} & \mathbf{v}^{\mathrm{T}} & \boldsymbol{\theta}^{\mathrm{T}} & \mathbf{m}_{op}^{\mathrm{T}} & \mathbf{m}_{tr}^{\mathrm{T}} & \mathbf{b}_{cent}^{\mathrm{T}} & b_{pd} \end{Bmatrix}^{\mathrm{T}} \tag{1}$$

where $\mathbf{r}$ is the inertial position of the vehicle with respect to the primary body, $\mathbf{v}$ is the corresponding inertial velocity with respect to the primary, $\boldsymbol{\theta}$ is the attitude error, $\mathbf{m}_{op}$ is the misalignment of the optical instrument, $\mathbf{b}_{tr}$ is the bias position of the instrument with respect to the navigation base, $\mathbf{b}_{cent}$ is the bias of the planetary centroid measurement, and b_{pd} is the bias of the planetary diameter measurement.

The nominal trajectory is obtained by integrating the nominal dynamics model with an Encke-Nystrom method.[4] Neither the attitude error $\delta\boldsymbol{\theta}$ nor its uncertainty are integrated in this analysis. The nominal attitude is known at any time and it does not need to be calculated. The attitude estimation error covariance is constant and is driven by the star tracker accuracy. The attitude navigation dispersion covariance is constant and is given by the attitude control dead-band. Before the star elevation is determined, the vehicle slews in preparation for measurement acquisition. This attitude maneuver is performed by the on-board thrusters and is assumed to be instantaneous. Due to thruster misalignment, this maneuver adds uncertainty to the translational states. After the batch of measurements is available, the vehicle returns to its nominal attitude. In linear covariance analysis, the difference between the true state and the nominal state is defined as the environment dispersion

$$\delta\mathbf{x} \triangleq \mathbf{x} - \bar{\mathbf{x}}. \tag{2}$$

The difference between the estimated state and the nominal state is defined as the navigation dispersion

$$\delta\hat{\mathbf{x}} \triangleq \hat{\mathbf{x}} - \bar{\mathbf{x}}. \tag{3}$$

Finally, the difference between the true state and the estimated state, is defined as the estimation error, sometimes referred to as the on-board navigation error

$$\mathbf{e} \triangleq \mathbf{x} - \hat{\mathbf{x}}. \tag{4}$$

Following the standard Kalman filter assumptions, the difference between the nominal and estimated models is represented with zero-mean, white noise. The estimated state evolves as

$$\dot{\hat{\mathbf{x}}} = \mathbf{f}(\hat{\mathbf{x}}), \tag{5}$$

where $\mathbf{f}$ is a nonlinear function representing the system dynamics as modeled by the filter. The evolution of the nominal state is modeled as

$$\dot{\bar{\mathbf{x}}} = \bar{\mathbf{f}}(\bar{\mathbf{x}}) = \mathbf{f}(\bar{\mathbf{x}}) + \boldsymbol{\upsilon}, \tag{6}$$

where $\bar{\mathbf{f}}$ is a nonlinear function representing the state dynamics as modeled in designing the nominal trajectory. The nominal dynamics $\bar{\mathbf{f}}$ may be higher fidelity than the filter's dynamics $\mathbf{f}$. The vector $\boldsymbol{\upsilon}$ represents the dynamics modeled in the nominal trajectory but neglected in the filter models. In Kalman filtering, the difference between the true dynamics and the filter's dynamics is called process noise. While these unmodeled dynamics are not actually white noise, they are modeled as such. The power spectral density of process noise is then tuned to achieve good performance. The same procedure is used here. In order to capture the difference between the two dynamical models, $\boldsymbol{\upsilon}$ is modeled as a zero-mean white noise process with power spectral density $\hat{\mathbf{Q}}$. The goal is to represent the increased value of the navigation dispersion during propagation due to the difference between the nominal and filter's dynamical models.

The evolution of the navigation dispersion can be approximated to first-order as

$$\delta\dot{\hat{\mathbf{x}}} = \dot{\hat{\mathbf{x}}} - \dot{\bar{\mathbf{x}}} = \mathbf{f}(\bar{\mathbf{x}} + \delta\hat{\mathbf{x}}) - \mathbf{f}(\bar{\mathbf{x}}) - \boldsymbol{\upsilon} \simeq \mathbf{F}(\bar{\mathbf{x}})\delta\hat{\mathbf{x}} - \boldsymbol{\upsilon}. \tag{7}$$

The evolution of the navigation dispersion covariance is governed by

$$\dot{\hat{\mathbf{P}}} = \mathbf{F}(\bar{\mathbf{x}})\hat{\mathbf{P}} + \hat{\mathbf{P}}\mathbf{F}(\bar{\mathbf{x}})^{\mathrm{T}} + \hat{\mathbf{Q}}. \tag{8}$$

Similarly, the true state is modeled to evolve as

$$\dot{\mathbf{x}} = \mathbf{f}(\mathbf{x}) + \boldsymbol{\nu}. \tag{9}$$

The evolution of the estimation error is given by

$$\dot{\mathbf{e}} = \dot{\mathbf{x}} - \dot{\hat{\mathbf{x}}} \simeq \mathbf{f}(\bar{\mathbf{x}}) + \mathbf{F}(\bar{\mathbf{x}})(\mathbf{x} - \bar{\mathbf{x}}) + \boldsymbol{\nu} - \mathbf{f}(\bar{\mathbf{x}}) - \mathbf{F}(\bar{\mathbf{x}})(\hat{\mathbf{x}} - \bar{\mathbf{x}}) = \mathbf{F}(\bar{\mathbf{x}})\mathbf{e} + \boldsymbol{\nu}. \tag{10}$$

Vector $\boldsymbol{\nu}$ is modeled as zero mean white noise with power spectral density $\mathbf{Q}$. The on-board covariance $\mathbf{P}$ evolves as

$$\dot{\mathbf{P}} = \mathbf{F}(\bar{\mathbf{x}})\mathbf{P} + \mathbf{P}\mathbf{F}(\bar{\mathbf{x}}) + \mathbf{Q}. \tag{11}$$

Notice that the Jacobian $\mathbf{F}$ could be evaluated at the estimated state $\hat{\mathbf{x}}$ instead of the nominal state $\bar{\mathbf{x}}$, as in the extended Kalman filter.

Finally

$$\delta\dot{\mathbf{x}} = \dot{\mathbf{x}} - \dot{\bar{\mathbf{x}}} \simeq \mathbf{F}(\bar{\mathbf{x}})\delta\mathbf{x} + \boldsymbol{\nu} - \boldsymbol{\upsilon} \tag{12}$$

and $\bar{\mathbf{P}}$ evolves as

$$\dot{\bar{\mathbf{P}}} = \mathbf{F}(\bar{\mathbf{x}})\bar{\mathbf{P}} + \bar{\mathbf{P}}\mathbf{F}(\bar{\mathbf{x}}) + \bar{\mathbf{Q}}. \tag{13}$$

Notice that $\bar{\mathbf{Q}} = \mathbf{Q} + \hat{\mathbf{Q}}$ if $\boldsymbol{\nu}$ and $\boldsymbol{\upsilon}$ are assumed to be uncorrelated.

THE ORION CISLUNAR NAVIGATION FILTER

The Filter States

The Orion on-board navigation filter will be required to estimate the position and velocity of the spacecraft. A decision has been made to separate out the attitude determination filter. It is important, however, to maintain an estimate of the attitude error of the vehicle since the measurements being taken are inherently angle measurements. Hence, navigation state vector is comprised of the following

$$\mathbf{x} = \begin{Bmatrix} \mathbf{r}^{\mathrm{T}} & \mathbf{v}^{\mathrm{T}} & \boldsymbol{\theta}^{\mathrm{T}} \end{Bmatrix}^{\mathrm{T}}. \tag{14}$$

where $\mathbf{r}$ is the inertial position of the vehicle with respect to the primary body, $\mathbf{v}$ is the corresponding inertial velocity with respect to the primary, and $\boldsymbol{\theta}$ is the attitude error.

The Filter Dynamics

Since this filter operates once Orion is away from Earth (and outside of GPS range), the primary forces governing the motion of the vehicle are the gravitational forces of the Earth, the Moon, and the Sun. The trajectory is designed taking into account all three of these bodies. Whereas the equations of motion are formulated with respect to a central body, this (central body) changes depending on which sphere of influence the vehicle is subject to.

The equations of motion for the Earth-Sun-Moon system are

$$\ddot{\mathbf{r}}_{PV} = -\frac{\mu_P}{r_{PV}^3}\mathbf{r}_{PV} - \mu_Q\left[\frac{\mathbf{r}_{QV}}{r_{QV}^3} + \frac{\mathbf{r}_{PQ}}{r_{PQ}^3}\right] - \mu_S\left[\frac{\mathbf{r}_{SV}}{r_{SV}^3} + \frac{\mathbf{r}_{PS}}{r_{PS}^3}\right] \tag{15}$$

where and $\mathbf{r}_{PV}$ is the position of the vehicle (V) with respect to the primary body (P), $\mathbf{r}_{QV}$ is the position of the vehicle with respect to the secondary body (Q), $\mathbf{r}_{PQ}$ is the position of the secondary body with respect to the primary body, $\mathbf{r}_{SV}$ is the position of the vehicle with respect to the Sun (S), and $\mathbf{r}_{PS}$ is the position of the Sun with respect to the primary body. The geometry is shown in Figure 1. In many applications, these equations are integrated by a Runge-Kutta or Runge-Kutta-Fehlberg fixed-step or variable-step algorithms.

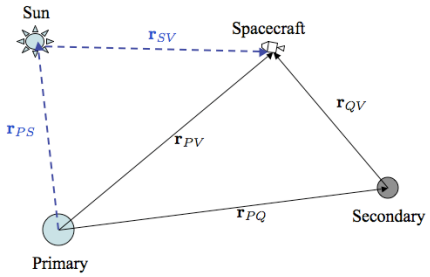

Figure 1. The Earth-Sun-Moon-Vehicle Geometry

The Measurements

Both 3-station and 6-station range and doppler measurement passes were used to construct a navigation translation state (position and velocity) solution (and covariance) which was then transmitted to the vehicle which then performed the maneuvers based upon these ground navigation updates.

System Model Parameters

Table 1 contains the data for the injection covariance matrix used in this analysis. Table 2 contains the model for the process noise used during the mission, both quiescent and active. Finally, Table 3 contains the maneuver execution errors for this case.

Error	Value
U (Radial) Position	30984.0 ft
V Position	196002.0 ft
W (Out-of-Plane) Position	10981.8 ft
U (Radial) Velocity	170.820 ft/s
V Velocity	29.250 ft/s
W (Out-of-Plane) Velocity	42.510 ft/s

Table 1. Translunar Injection Accuracy (3σ)

Type	Value
Quiescent	3.801×10^{-8} ft^2/s^3
Active (CM/SM)	1.410×10^{-4} ft^2/s^3
Active (CM only)	8.479×10^{-4} ft^2/s^3

Table 2. Vehicle Translation Process Noise Characteristics

Concept of Operations of Maneuvers and Ground Navigation Passes

Four outbound trajectory correction (OTC) maneuvers will be performed on the leg from the Earth to the Moon, a single Outbound Powered Flyby (OPF) maneuver targeting for the DRO insertion point, two outbound correction maneuvers between the OPF and the DRO Insertion (DRO-I) point. Once on the DRO, three (DRO) Orbit Maneuvers (OM) spaced approximately equally, all targeting the DRO Departure maneuver point are performed. After the DRO Departure (DRO-D) maneuver, there are two correction maneuvers targeting the perilune conditions of the Return Powered Flyby (RPF) maneuver. Finally, at after RPF, there are three correction maneuvers (RTC 4-6). These maneuvers and their TIGs are outlined in Table 4.

The *nominal* ground navigation network was assumed to be a 6-station configuration (Goldstone, Madrid, Canberra, Hartebeestoek, Santiago, Usuda). The ground navigation passes were chosen so as to upload the state to the vehicle 1 hour before each maneuver. This was to allow for the final targeting of the maneuver as well as time to perform an attitude maneuver to get to the maneuver attitude. During those epochs when the maneuvers occured more than 24 hours apart, ground navigation passes were scheduled so as to ensure that the on-board state remained reasonable.

THE NAVIGATION ERRORS AND TRAJECTORY DISPERSIONS

The EM-1 Mission is divided into five phases: the Earth-Moon (TransLunar) Phase, the Moon-to-DRO phase, the DRO-orbit phase, the DRO-to-Moon phase and the Moon-to-Earth (transEarth) phase. Whereas the navigation errors and trajectory dispersions are important in each phase, of particular importance are the Earth-to-Moon, DRO-to-Moon and the Moon-to-Earth phases. Of ultimate importance is the Moon-to-Earth Phase because that determines whether the crew can return safely to Earth. Of course, the epoch of concern in this phase is the Entry Interface (EI) condition. In what follows the trajectory dispersions and navigation errors in each of these three

Maneuver Execution Error	3σ Value
Noise (ft/s)	0.027
Bias (ft/s)	0.009
Scale Factor (ppm)	450.0
Misalignment (deg)	0.03

Table 3. The Maneuver Execution Error Model

phases will be detailed.

Translunar Phase

The navigation errors and trajectory dispersions mapped to the B-plane are presented in Figures 2-3. The time history of the linearized time of flight of the navigation errors and the trajectory dispersions are presented in Figures 4-5. The trajectory dispersions at the time of the OPF maneuver are presented in Table 5. The B-plane trajectory dispersions at the time of the OPF maneuver are presented in Table 6.

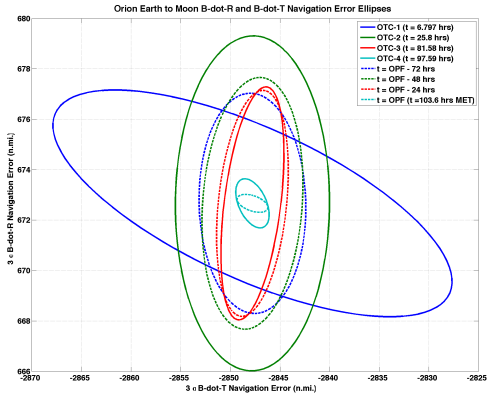

Figure 2. Translunar Navigation Errors mapped to the B-plane

The Trans-DRO Orbit Phase

The navigation errors mapped to the time of the DRO Insertion Maneuver are presented in Figures 6-7. The trajectory dispersions mapped to the time of the DRO Insertion Maneuver are presented in Figures 8-9. We have displayed the navigation errors and the trajectory dispersions mapped to this epoch because these are the quantities that are being targeted.

The DRO Orbit Phase

The navigation errors mapped to the time of the DRO Departure Maneuver are presented in Figures 10-11. The trajectory dispersions mapped to the time of the DRO Departure Maneuver are

Maneuver #	Type	t_{ig} (hrs)	$\|\Delta V_{nom}\|$ (ft/s)
1	OTC-1	6.81	0.000
2	OTC-2	25.81	0.000
3	OTC-3	81.60	0.000
4	OTC-4	97.60	0.000
5	OPF	103.60	572.627
6	OTC-5	122.41	0.000
7	OTC-6	144.00	0.000
8	DRI	169.21	797.479
9	OM-1	204.00	0.000
10	OM-2	240.00	0.000
11	OM-3	276.00	0.000
12	DRD	316.80	278.567
13	RTC-1	372.01	0.000
14	RTC-2	426.01	0.000
15	RTC-3	477.62	0.000
16	RPF	483.62	827.866
17	RTC-4	501.61	0.000
18	RTC-5	591.04	0.000
19	RTC-6	607.04	0.000
Total			**2476.539**

Table 4. The Maneuver Plan

presented in Figures 12-13. As in the trans-DRO phase, the navigation errors and the trajectory dispersions are mapped to this epoch because these are the quantities that are being targeted.

The DRO-to-Moon Phase

The navigation errors and trajectory dispersions mapped to the B-plane are presented in Figures 14-15. For a sense of scale, these navigation errors and trajectory dispersions mapped to the B-plane with the (radius of the) Moon plotted for scale are presented in Figures 16-17. The navigation errors at the time of the RPF maneuver are presented in Table 7. The trajectory dispersions at the time of the RPF maneuver are presented in Table 8.

The Trans-Earth Phase

The navigation errors mapped to Entry Interface flight path angle errors are presented in Figures 18. The trajectory dispersions mapped to Entry Interface flight path angle trajectory dispersions are presented in Figures 19. Figures 20-22 contain the trajectory dispersion ellipses mapped to EI so that the correlations between the components (Downrange Position and Flight Path Angle, Velocity Magnitude and Flight Path Angle, and Crossrange Position and Crossrange Velocity) are observedThese plots also have the EI requirement displayed. One can see that that the requirement for Velocity Magnitude and Flight Path Angle is violated. The major contributor to this violation is the late ammonia sublimator vent that occurs 0.5 hour before EI.

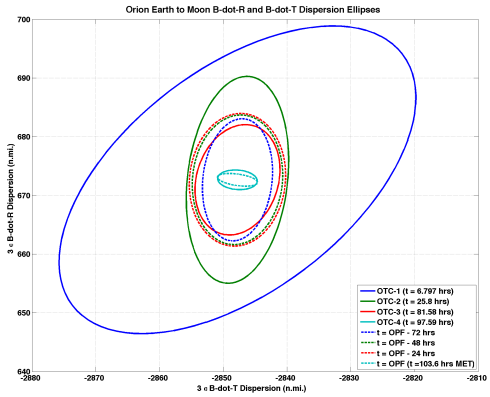

Figure 3. Translunar Trajectory Dispersion mapped to the B-plane

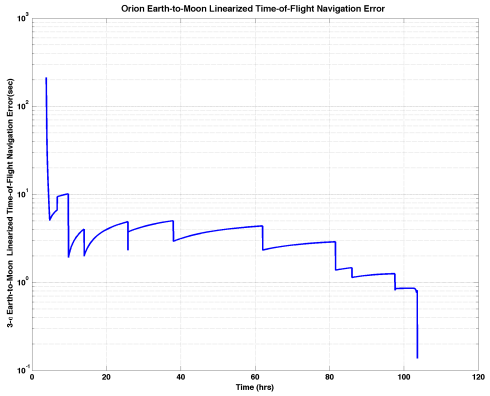

Figure 4. Translunar Navigation Errors mapped to the B-plane Linearized Time-of-Flight (T_L)

Summary Statistics for the EM-1 (DRO) Mission

Table 9 contains the $|\Delta \mathrm{V}|$ statistics for this Maneuver Profile. The quantity $|\Delta \mathbf{V}|_{99.73}$ represents the $|\Delta \mathbf{V}|$ values, 99.73% of samples of which are below this value (for a univariate Gaussian distribution $\Pr(\mu - 3\sigma \leq x \leq \mu + 3\sigma) \approx .9973$). In order to determine this, the covariance was sampled 10,000 times and from this the $|\Delta \mathbf{V}|_{99.73}$ and the other statistics (μ and σ of the $|\Delta \mathbf{V}|$) were computed.[5]

Table 14 contains the delivery statistics at the EI point.

Finally, Table 15 determines whether the dispersion ellipse EI requirements[6] are satisfied the EI point. The partials of these quantities are somewhat involved.[7] Margin is defined in terms of the following equation

$$\text{Margin} = \begin{cases} (\sqrt{N} - 1) * 100, & N \geq 1 \\ (1 - \frac{1}{\sqrt{N}}) * 100, & N < 1 \end{cases} \tag{16}$$

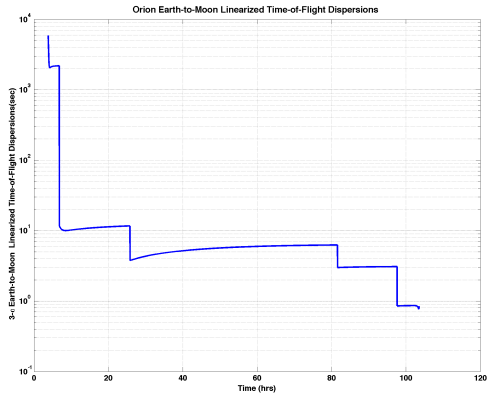

Figure 5. Translunar Trajectory Dispersion mapped to the B-plane Linearized Time-of-Flight (T_L)

Type	Pericynthion 3σ Value
Periapsis Altitude	1.0077 n.m.
Inclination	0.0162 deg
Argument of Periapsis	0.1168 deg
C_3	26307.2755 $\mathrm{ft}^2/\mathrm{s}^2$

Table 5. The Trans-Lunar Delivery 3σ Statistics at OPF

where N is the multiplier on the Dispersion covariance such that it is tangential to the requirement.

One can see from the Table and (particularly) from the Figures (40-42) that with respect to the Velocity Magnitude Vs Flight Path Angle, that the requirement is violated in the velocity magnitude component, but only in terms of the orientation of the ellipse. There is adequate margin in the Flight Path Angle component of the requirement.

STATISTICS FOR THE VARIATION IN THE NUMBER OF GROUND STATIONS

This section presents the analysis when the ground stations were varied from 3 to 9, in increments of 3. The 3 station configuration contains the 3 DSN stations: Goldstone, Madrid, and Canberra. The 9 station configuration includes the sites in the 6 station network and includes Diego Gracia, Hawaii and Ascencion Island. Table 12 contains the $|\Delta\mathbf{V}|$ statistics for when the number of ground stations is varied.

Finally, Table 13 contains the delivery statistics at the EI point for each of these cases when the number of ground stations is varied.

Statistics for the Variation in the Ammonia Sublimator Noise

The Ammonia Sublimator is a major contributor to the EI delivery accuracy. The final vent occurs 1/2 hour before EI and continues until EI. To that end, the sublimator noise is varied. The nominal maneuver noise is 8.479 $\times 10^{-4}$ $\mathrm{ft}^2/\mathrm{s}^3$ (1σ). From this, the maneuver noise is varied between the

Type	Pericynthion 3σ Value
$\mathbf{B}\cdot\mathbf{T}$	5.4367 n.m.
$\mathbf{B}\cdot\mathbf{R}$	1.8584 n.m.
Linearized Time-of-Flight	0.8421 sec

Table 6. The Trans-Lunar Delivery 3σ B-plane Statistics at OPF

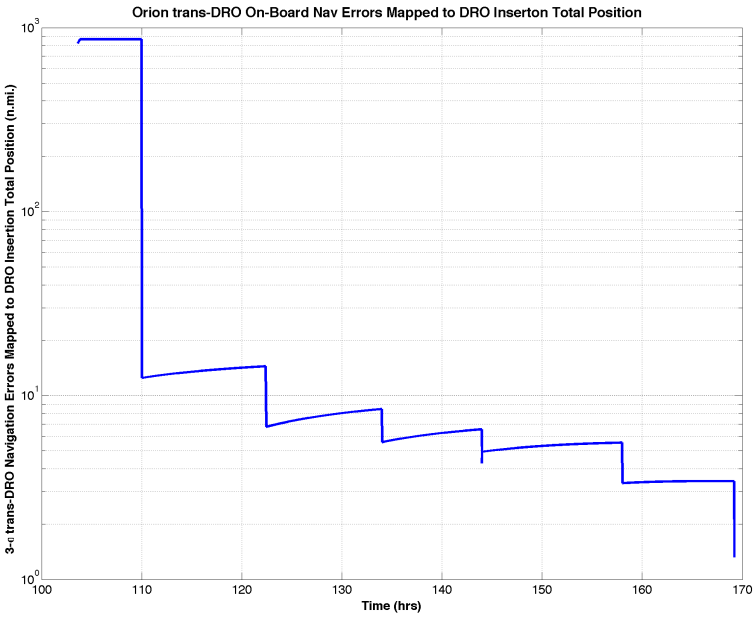

Figure 6. The Trans-DRO Orbit on-board Navigation Error Mapped to DRO Insertion Position Error

CM/SM strength of 8.479 $\times 10^{-4}$ ft^2/s^3 and its quiscent strength of 3.801 $\times 10^{-8}$ ft^2/s^3 (1σ). Table 15 contains the delivery statistics at the EI point for each of these cases when the maneuver noise is varied. Finally, the margin for each of these cases is tabulated in Table 16.

CONCLUSIONS AND RECOMMENDATIONS

This paper details the linear covariance analysis for the EM-1 DRO mission with ground-based navigation updates. The sensitivity analysis shows that having 6 ground stations available for navigation tracking improves the trajectory dispersions at EI (as compared to 3 stations), not to mention the $|\Delta\mathbf{V}|$ dispersions. The major contributor to EI delivery accuracy is the sublimator vent just prior to EI. Were the strength of that vent reduced, the EI accuracy requirements would be satisfied.

Acknowledgements

Many thanks to Sara Scarritt for generating the Lincov maneuver partials and to Dave Woffinden for many helpful discussions.

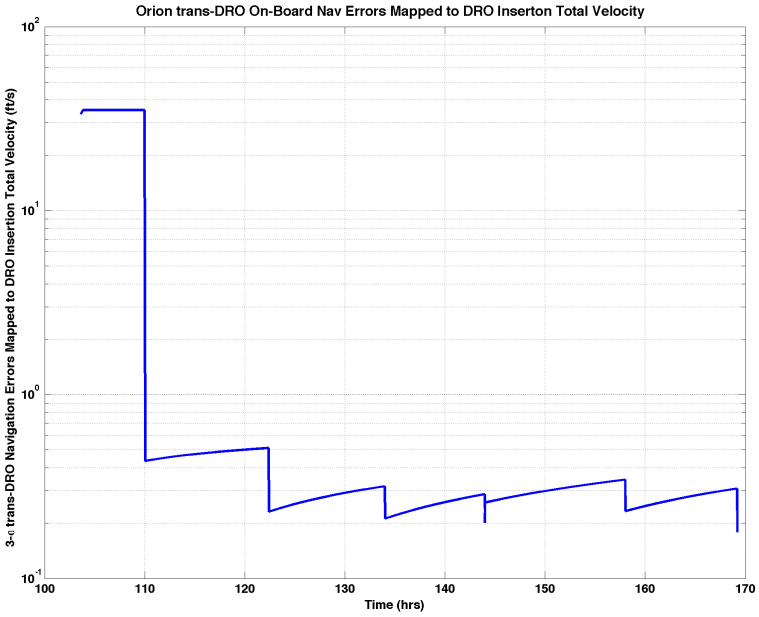

Figure 7. The Trans-DRO Orbit on-board Navigation Error Mapped to DRO Insertion Velocity Error

Type	RPF 3σ Value
Periapsis Altitude	0.1675 n.m.
Inclination	0.0060 deg
Argument of Periapsis	0.1227 deg

Table 7. The DRO-to-Moon Navigation Error 3σ Statistics at RPF

REFERENCES

[1] P. Maybeck, *Stochastic Models, Estimation and Control, Vol. 1*. New York, NY: Academic Press, 1979.

[2] C. D'Souza and R. Zanetti, "Navigation Design and Analysis for the Orion Earth-Moon Mission," *AAS/AIAA Space Flight Mechanics Conference*, February 2014.

[3] D. K. Geller, "Linear Covariance Techniques for Orbital Rendezvous Analysis and Autonomous Onboard Mission Planning," *Journal of Guidance, Navigation and Dynamics*, Vol. 29, No. 6, 2006, pp. 1404–1414.

[4] R. Battin, *An Introduction to the Mathematics and Methods of Astrodynamics*. Reston, VA: AIAA, 1999.

[5] W. Bollman and C. Chadwick, "Statistics of ΔV Magnitude for a Trajectory Correction Maneuver Containing Deterministic and Random Components," *Proceedings of the AIAA/AAS Astrodynamics Conference*, August 1982.

[6] J. Rea, "Entry Interface Accuracy Requirements for Exploration Mission Critical Design Review," EG Technical Brief, FltDyn-CEV-15-28, Johnson Space Center, Engineering Directorate, Houston, TX, July 2015.

[7] C. D'Souza, "Mapped Terminal Trans-Lunar and Trans-Earth Conditions for the Orion Cislunar Missions," EG Technical Brief, FltDyn-CEV-15-017, Johnson Space Center, Engineering Directorate, Houston, TX, May 2015.

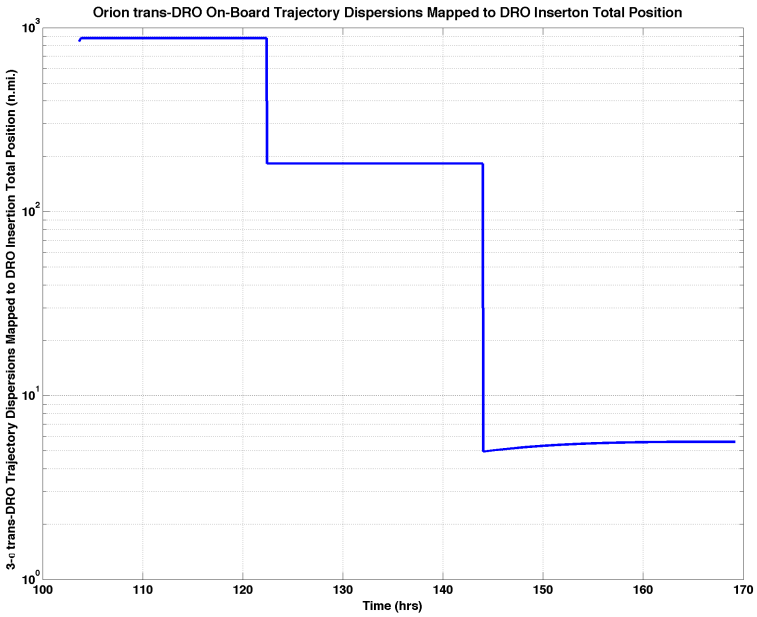

Figure 8. The Trans-DRO Orbit Trajectory Dispersions Mapped to DRO Insertion Position Dispersion

Type	RPF 3σ Value
Periapsis Altitude	0.8527 n.m.
Inclination	0.0107 deg
Argument of Periapsis	0.2721 deg

Table 8. The DRO-to-Moon Delivery 3σ Statistics at RPF

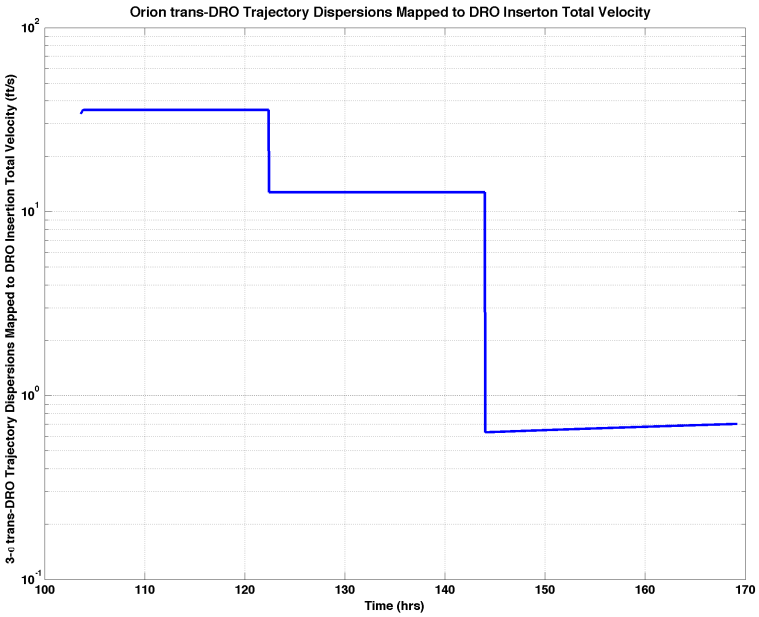

Figure 9. The Trans-DRO Orbit Trajectory Dispersions Error Mapped to DRO Insertion Velocity Dispersion

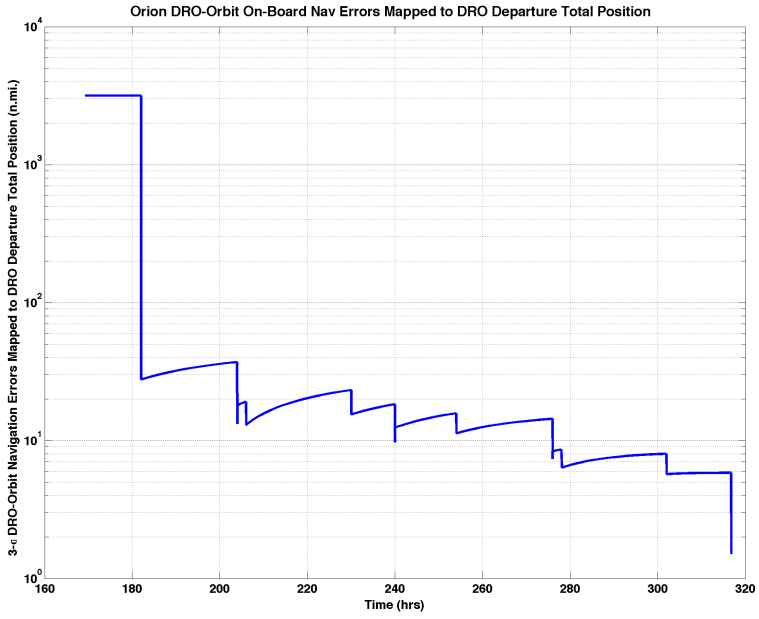

Figure 10. The DRO Orbit on-board Navigation Error Mapped to DRO Departure Position Error

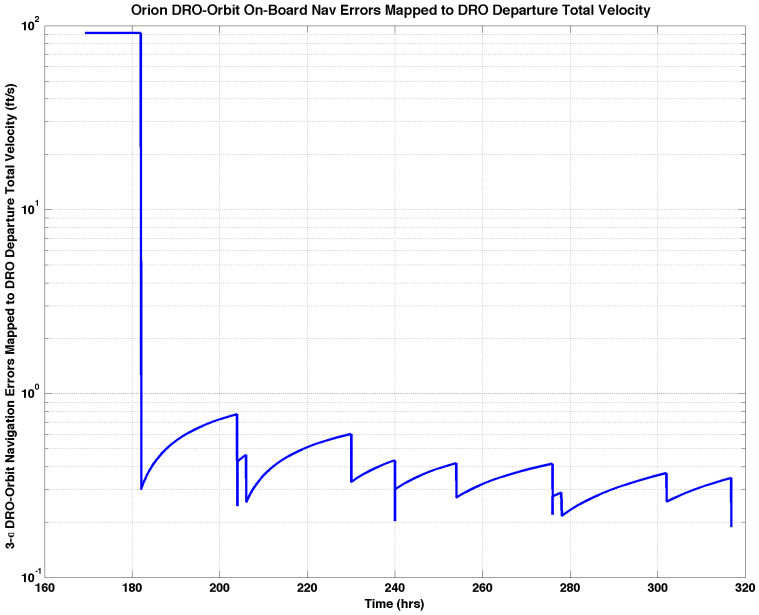

Figure 11. The DRO Orbit on-board Navigation Error Mapped to DRO Departure Velocity Error

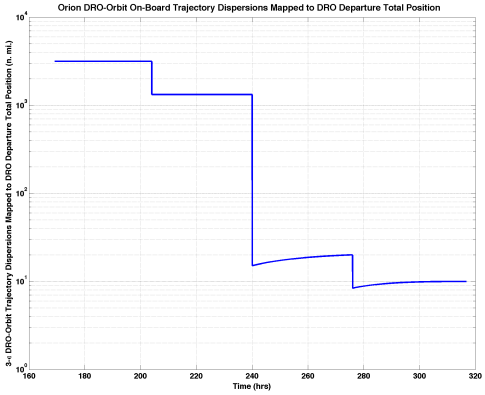

Figure 12. The DRO Orbit Trajectory Dispersions Mapped to DRO Departure Position Dispersion

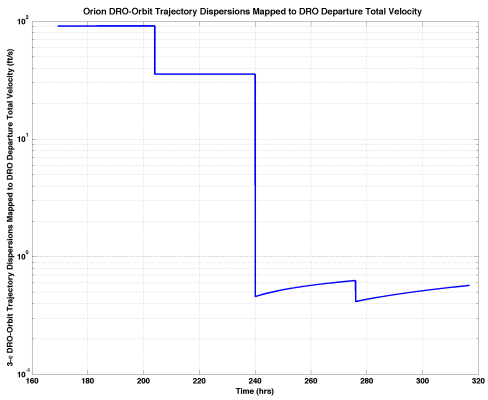

Figure 13. The DRO Orbit Trajectory Dispersions Error Mapped to DRO Departure Velocity Dispersion

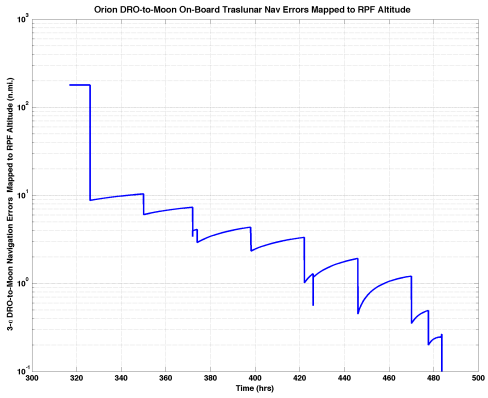

Figure 14. DRO-to-Moon Navigation Errors Mapped to the Errors in Pericynthion Radius

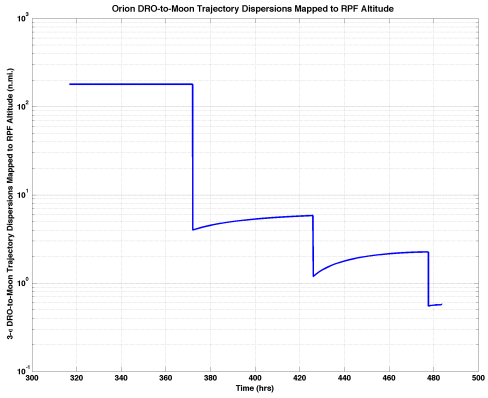

Figure 15. DRO-to-Moon Trajectory Dispersion Mapped to the Errors in Pericynthion Radius

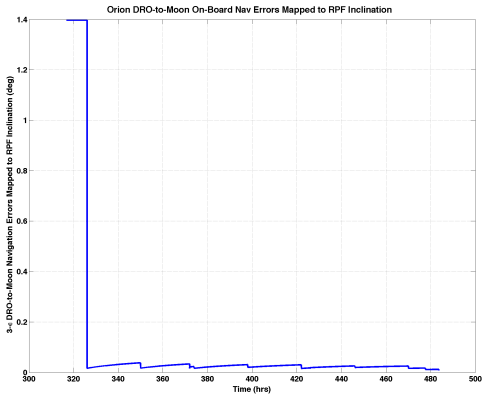

Figure 16. DRO-to-Moon Navigation Errors mapped to the Errors in Pericynthion Inclination

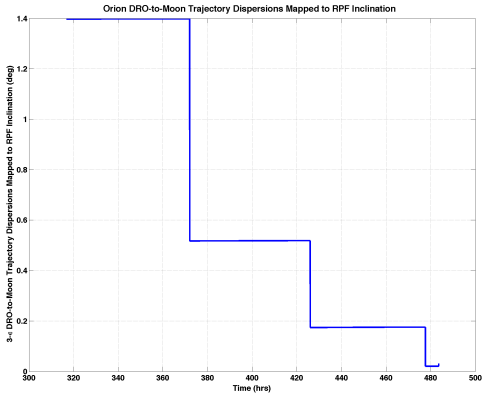

Figure 17. DRO-to-Moon Trajectory Dispersion mapped to Errors in Pericynthion Inclination)

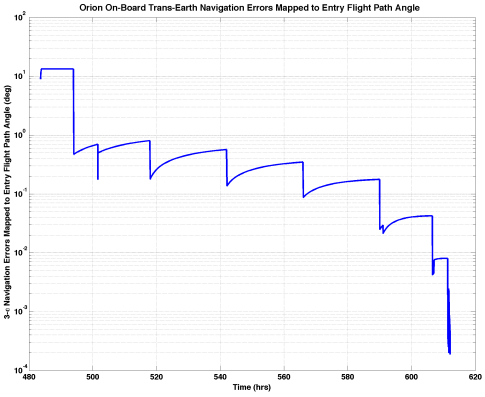

Figure 18. The on-board Navigation Errors Mapped to Entry Interface Flight Path Angle Errors

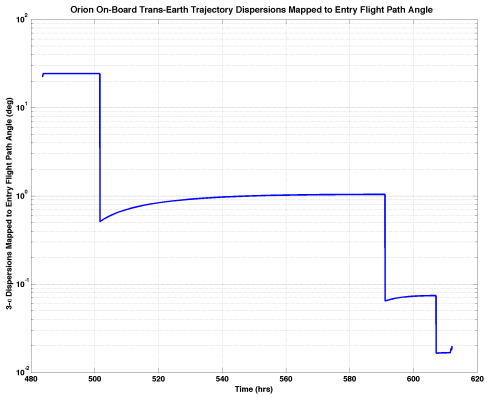

Figure 19. The Trans-Earth Trajectory Dispersions Mapped to Entry Interface Flight Path Angle Dispersions

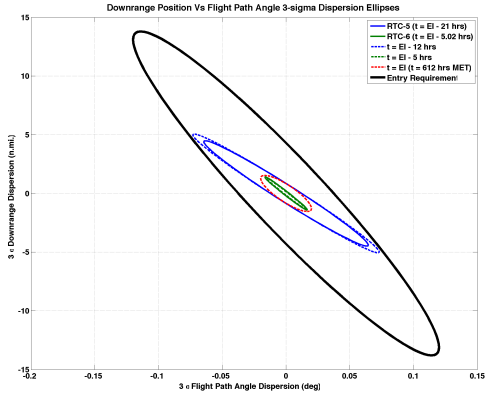

Figure 20. The Trans-Earth Entry Interface Conditions Mapped Downrange vs Flight Path Angle Trajectory Dispersion Ellipses

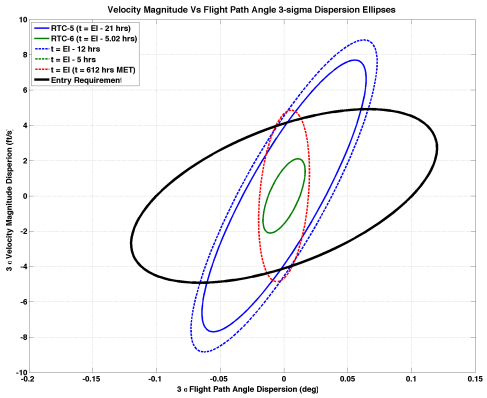

Figure 21. The Trans-Earth Entry Interface Conditions Mapped Velocity Magnitude vs Flight Path Angle Trajectory Dispersion Ellipses

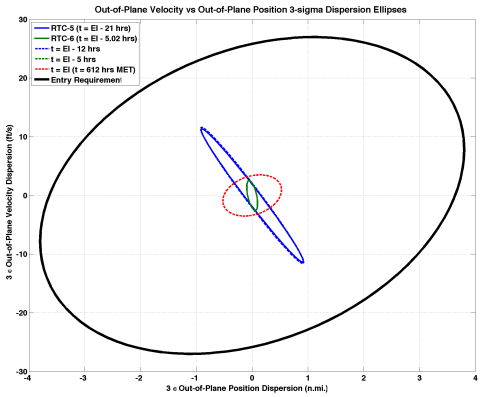

Figure 22. The Trans-Earth Entry Interface Conditions Mapped Crossrange Positon vs Crossrange Velocity Trajectory Dispersion Ellipses

Maneuver #	Type	t_{ig} (hrs)	$\|\Delta\mathbf{V}\|_{nom}$ (ft/s)	$\mu_{\|\Delta\mathbf{V}\|}$ (ft/s)	$\sigma_{\|\Delta\mathbf{V}\|}$ (m/s)	$\|\Delta\mathbf{V}\|_{99.73}$ (ft/s)
1	OTC-1	6.81	0.000	13.357	8.811	46.666
2	OTC-2	25.81	0.000	0.208	0.107	0.574
3	OTC-3	81.60	0.000	0.463	0.207	1.170
4	OTC-4	97.60	0.000	0.791	0.376	2.133
5	OPF	103.60	572.627	572.714	1.888	578.728
6	OTC-5	122.41	0.000	4.214	3.084	15.377
7	OTC-6	144.00	0.000	1.680	1.070	5.533
8	DRI	169.21	797.479	797.478	0.122	797.805
9	OM-1	204.00	0.000	1.312	0.660	3.616
10	OM-2	240.00	0.000	0.688	0.332	1.870
11	OM-3	276.00	0.000	0.222	0.094	0.551
12	DRD	316.80	278.567	278.567	0.106	278.849
13	RTC-1	372.01	0.000	0.446	0.233	1.333
14	RTC-2	426.01	0.000	0.259	0.112	0.647
15	RTC-3	477.62	0.000	1.209	0.814	4.302
16	RPF	483.62	827.866	827.869	0.471	829.190
17	RTC-4	501.61	0.000	1.741	1.078	5.938
18	RTC-5	591.04	0.000	0.862	0.492	2.634
19	RTC-6	607.04	0.000	0.523	0.252	1.382
Total			**2476.539**	**2504.604**		**2578.300**

Table 9. The $|\Delta\mathrm{V}|$ Statistics

Type	Entry Interface 3σ Value
Latitude	0.0444 deg
Longitude	0.0097 deg
Flight Path Angle	0.0199 deg
Heading Angle	0.0286 deg

Table 10. The Final Delivery 3σ Statistics

Type	PASS / FAIL	Margin
Downrange Position Vs Flight Path Angle	PASS	220.8044
Velocity Magnitude Vs Flight Path Angle	FAIL	-15.5571
Velocity Magnitude Vs Downrange Position	FAIL	-20.0120
Velocity Magnitude Vs Flight Path Angle	PASS	621.5096

Table 11. The EI Requirement Satisfaction

				6 Ground Stations	3 Ground Stations	9 Ground Stations
Man #	Type	t_{ig} (hrs)	$\|\Delta\mathbf{V}\|_{nom}$ (ft/s)	$\|\Delta\mathbf{V}\|_{99.73}$ (ft/s)	$\|\Delta\mathbf{V}\|_{99.73}$ (ft/s)	$\|\Delta\mathbf{V}\|_{99.73}$ (ft/s)
1	OTC-1	6.81	0.000	46.666	46.666	46.666
2	OTC-2	25.81	0.000	0.574	0.574	0.574
3	OTC-3	81.60	0.000	1.170	1.171	1.169
4	OTC-4	97.60	0.000	2.133	2.128	2.128
5	OPF	103.60	572.627	578.728	578.638	578.361
6	OTC-5	122.41	0.000	15.377	15.804	15.089
7	OTC-6	144.00	0.000	5.533	5.723	5.400
8	DRI	169.21	797.479	797.805	797.811	797.804
9	OM-1	204.00	0.000	3.616	3.618	3.616
10	OM-2	240.00	0.000	1.870	1.875	1.870
11	OM-3	276.00	0.000	0.551	0.553	0.544
12	DRD	316.80	278.567	278.849	278.850	278.848
13	RTC-1	372.01	0.000	1.333	1.332	1.334
14	RTC-2	426.01	0.000	0.647	0.666	0.639
15	RTC-3	477.62	0.000	4.302	4.322	4.291
16	RPF	483.62	827.866	829.190	829.189	829.190
17	RTC-4	501.61	0.000	5.938	5.938	5.939
18	RTC-5	591.04	0.000	2.634	2.638	2.633
19	RTC-6	607.04	0.000	1.382	1.393	1.378
Total			**2476.539**	**2578.300**	**2578.889**	**2577.472**

Table 12. $|\Delta\mathbf{V}|$ Statistics for the Variation of the Number of Ground Stations

EI Delivery Error	Nominal	Case 1	Case 2
Latitude (3σ)	0.044°	0.047°	0.044°
Longitude (3σ)	0.010°	0.010°	0.010°
Flight Path Angle (3σ)	0.020°	0.021°	0.020°
Heading Angle (3σ)	0.029°	0.030°	0.028°

Table 13. The Final Entry Interface 3σ Delivery Statistics as a Function of the Variation of the Number of Ground Stations

Type	Nominal Case	3 Ground Stations	9 Ground Stations
Downrange Position Vs Flight Path Angle	220.804	209.520	222.977
Velocity Magnitude Vs Flight Path Angle	-15.557	-23.512	-14.523
Velocity Magnitude Vs Downrange Position	-20.012	-28.823	-18.849
Crossrange Positon Vs Crossrange Velocity	621.510	598.443	625.797

Table 14. Requirement Satisfaction for the Variation of the Number of Ground Stations

EI Delivery Error	Nominal	SM/CM Sublimator Noise	Quiescent Sublimator Noise
Latitude (3σ)	0.044°	0.043°	0.042°
Longitude (3σ)	0.010°	0.004°	0.002°
Flight Path Angle (3σ)	0.020°	0.017°	0.016°
Heading Angle (3σ)	0.029°	0.026°	0.026°

Table 15. The Final Entry Interface 3σ Delivery Statistics as a Function of the Variation of Sublimator Noise

Type	Nominal Case	SM/CM Noise	Quiescent Noise
Downrange Position Vs Flight Path Angle	220.804	419.469	499.159
Velocity Magnitude Vs Flight Path Angle	-15.557	59.293	116.517
Velocity Magnitude Vs Downrange Position	-20.012	51.533	103.562
Crossrange Positon Vs Crossrange Velocity	621.510	910.442	949.406

Table 16. Requirement Satisfaction for the Variation of the Sublimator Noise